JOURNAL OF MATERIALS SCIENCE 27 (1992) 4751–4761

Grain-size effects in the indentation fracture of MgO

R. F. COOK, E. G. LINIGER
IBM Research Division, T. J. Watson Research Center, Yorktown Heights, NY 10598, USA

The variation of radial crack length with indentation load in a series of polycrystalline MgO materials is examined as a function of grain size. Comparison with the single-crystal response indicates that the fracture resistance of the polycrystals is significantly enhanced. Fracture surface observations suggest that the source of the enhancement is frictional interlocking of jogs in the crack plane caused by the tendency of the local crack path to maintain preferred crystalline cleavage planes. A model is developed for the fracture resistance increase and used to describe the radial crack lengths. The parameters thus derived suggest that a minimum grain size exists, below which this mechanism of fracture resistance is not operative.

1. Introduction

Implicitly or explicitly recognized in many studies considering microstructural influences on strength in polycrystalline ceramics is the fact that the precursor cracks ultimately responsible for strength control are also under microstructural toughening influences, before any propagation associated with the failure process [1–12]. However, little analysis [1, 4] has been made of the effects of microstructure on stable equilibrium crack lengths in ceramics toughened by either ligamentary bridging or phase transformation processes. In particular, analysis of the lengths of stable cracks generated at indentations, frequently used in strength and toughness assessments [1–3, 5–7, 9, 10], and often thought to model "natural" or "intrinsic" flaws, has not been made.

The two components of the fracture equation determining an equilibrium indentation crack length are the applied mechanical energy release rate, $\mathcal{G}_a$, driving the crack and the fracture resistance, R, characterizing the work necessary for crack advance. Microstructure, and hence grain size, may influence the magnitude and crack-length dependence of both $\mathcal{G}_a$ and R. In this paper we focus on the grain-size dependence of R, assuming $\mathcal{G}_a$ to be independent of grain size. A model is developed for the stable equilibrium lengths of indentation radial cracks generated in a material toughened by ligamentary bridges, motivated in part by experimental observations of the indentation cracking patterns observed in a series of polycrystalline MgO materials. The responses predicted by the model are fitted to the observed radial crack lengths, allowing transient R curves to be generated.

2. Experimental details and observations

2.1. Materials

Polycrystalline, opaque MgO (Ozark Technical Ceramics, Inc., Webb City, MO, USA) was obtained in the form of discs 32 mm × 4 mm, slip cast from a powder mixture consisting of 98 wt % MgO and 2 wt % Y_2O_3 and sintered to 97.5% of theoretical density. The as-received discs were given additional heat treatments at 1600 °C in air for 0, 4, 16, or 48 h, generating four microstructures in all. To insure that both faces were parallel and smooth, the discs were machined and polished with progressively finer grits, the finest of which was colloidal silica (0.05 μm). The discs were then annealed at 1200 °C for 2 h to remove any residual stress due to machining [13] and to thermally etch the grain boundaries. For reference purposes a polycrystalline, translucent, fully dense MgO specimen (Avco Corporation, Wilmington, MA, USA), 12 mm × 5 mm × 2 mm, and a (1 0 0) single crystal of MgO (Norton Research, Niagra Falls, Ontario, Canada) 12 mm × 12 mm × 3 mm, were obtained and similarly machined, polished and annealed.

Fig. 1 shows optical micrographs of the polished polycrystalline surfaces, indicating an increase in grain size and reduction in porosity with increasing heat treatment. Table I gives the mean grain-boundary intercept length, λ, and relative density, ρ, determined for each material. Much more extensive grain growth has been observed for other MgO materials [14–16] than the factor of 2.5 observed here after 48 h at 1600 °C. The relative retardation in our materials is attributed to pore drag on the grain boundaries (very evident in Fig. 1c and d), and possibly solute drag by Y-segregation to the boundaries or impurity pinning (X-ray diffraction suggested the possible formation of the MgY_2O_4 spinel in the microstructure).

2.2. Testing

Specimens were indented by using a Vickers diamond pyramid over the peak-load range 0.25–200 N with a dwell time of 15 s. The single-crystal specimen was

0022–2461 © *1992 Chapman & Hall*

TABLE I Microstructural and fracture parameters of MgO (H-values are ± 10%)

Material	λ (μm)	ρ (%)	H (GPa)	P^* (N)	l^M (μm)	$R_\infty/2\gamma$	δ (μm)
Polycrystals							
No heat treatment	9.2	97.5	5.78	0.054	0.25	2.29	2.20
4 h heat treatment	12	97.8	5.78	0.059	0.29	2.16	2.61
16 h heat treatment	17	98.7	6.08	0.132	0.62	2.26	5.55
48 h heat treatment	26	98.7	6.37	0.368	1.41	2.77	8.87
Single crystal	–	100	6.30	–	–	1	–

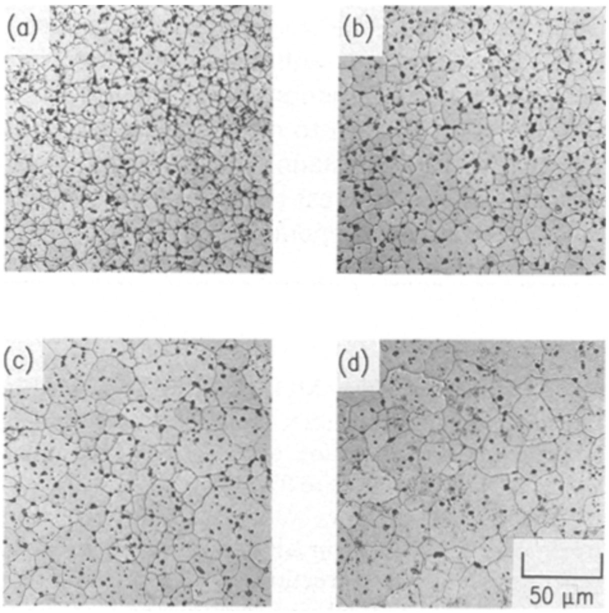

Figure 1 Optical micrographs (reflected light) of polished and thermally etched surfaces of polycrystalline MgO materials. Increasing heat treatment is shown in the sequence (a)–(d).

oriented such that the primary radial cracks generated at the indentation propagated parallel to the indentation diagonals. Although {1 0 0} cleavage is favoured in macroscopic fracture specimens of MgO [17, 18], dislocation interactions at indentations predominantly generate and stabilize cracks on {1 1 0} planes [19–26] (similar to those generated at intersecting slip bands in compression and bend specimens [27, 28]). Thus the primary radial cracks generated in the single crystal here were thought to lie on {1 1 0} planes, and the smaller, secondary radials, also initiated at the indentation corners, on the {1 0 0} planes.

Observations using an inverted tester [29] on the polycrystalline translucent MgO showed that cracks (radial and lateral) were initiated almost immediately during the indentation loading cycle, and grew on continued loading, similar to the behaviour of single-crystal MgO [29]. The lateral cracks extended significantly during unloading. Also similar to single-crystal MgO and other single crystals and polycrystals [29, 30], the radial cracks observed in this polycrystalline MgO had no significant subsurface trace beneath the contact impression. Cross-sections of indentations [20, 25] and observations of impact craters [22, 23] in single-crystal MgO are consistent with these observations of shallow radial and lateral cracks. Acoustic emission measurements [26] during indentation of single-crystal MgO also support the observations of crack initiation during loading.

Fig. 2 shows the indentation crack morphology observed in the above cases, and assumed to pertain to the opaque materials examined here. The contact impression dimension, a, radial crack surface-trace dimension, l, and lateral crack development, were measured over the range of indentation loads by using bright field, dark field, and Nomarski contrast optical microscopy. Fracture surfaces of indented bar specimens cut from the discs were examined by scanning electron microscopy.

2.3. Indentation and fracture morphology

Micrographs of 1 N and 50 N indentation in the 16 h heat-treated material are shown in Fig. 3a and b, and represent the two extremes of observed behaviour. The contact impression and associated radial cracks are small relative to the grain dimensions for the 1 N indentation, and the properties which control the indentation morphology are dominated by those of the single crystal. In particular, the strong influence of the tendency to {1 0 0} and {1 1 0} cleavage is seen in the fact that the radial cracks do not emanate from the corners of the contact impression or propagate collinear with the impression diagonals. The contact

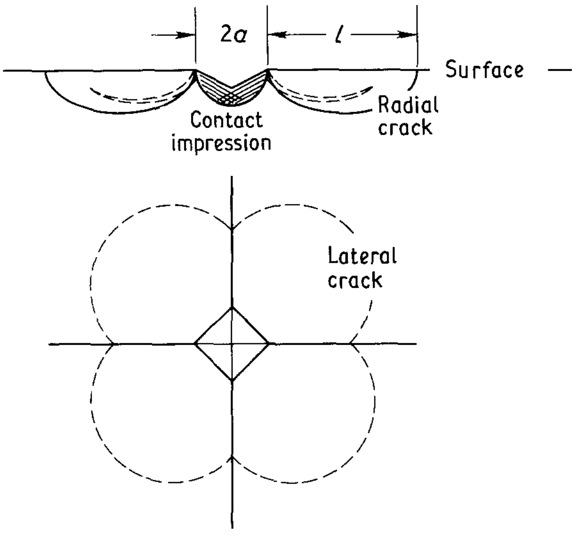

Figure 2 Cross-section and plan views of indentation crack system, showing radial and lateral crack morphologies and defining contact impression dimension, a, and radial crack surface-trace dimension, l.

impression and radial cracks for the 50 N indentation are several times larger than the grain size, and the indentation morphology now reflects the cumulative influences of the crystalline anisotropy and microstructural inhomogeneity. The radial cracks, in this case as well, have not initiated at the impression corners and do not propagate collinear with the impression diagonals, and additionally, appear to be detached from the contact impression, exhibit discontinuous surface traces, and are relatively shorter than their 1 N counterparts. Considerable lateral cracking is also observed. Fig. 3c shows the surface trace of a radial crack generated at a 50 N indentation. The trace is relatively straight and exhibits no apparent interaction between the crack and the grain boundaries or grain anisotropy. This observation is in strong contrast to that for polycrystalline Al_2O_3 [1, 31, 32], but is similar to that for polycrystalline Y_2O_3 [33].

Fig. 4 plots the contact dimension a against indentation load P for the four polycrystalline materials. Over the range of contact loads studied all four materials exhibited a $P^{1/2}$ load dependence indicative of constant hardness, H:

$$a = (P/2H)^{1/2} \tag{1}$$

The solid lines in Fig. 4 are best fits to the data in accord with Equation 1. Table I gives the hardness values thus derived. Notably, the polycrystalline hardness values are only marginally depressed from the value determined for the single crystal over the same load range (Table I), consistent with increased porosity, and the a values for the polycrystals do not deviate from the constant hardness lines for impression dimensions less than the grain size λ (Fig. 4). Slip band traces were observed in grains adjacent to the contact impression in all the polycrystalline materials at all indentation loads. An example is shown in Fig. 5. The traces were grain localized and randomly oriented with respect to the indentation, reflecting the preferred $\{1\,1\,0\}\langle 1\,1\,0\rangle$ slip systems of individual grains. Such changes in orientation of the traces from grain to grain are similar to the changes in direction of lines of dislocation etch-pits across subgrain boundaries [20]. No slip traces were observed on the indented single-crystal surfaces. The grain-size invariance of polycrystalline hardness and similarity with the single-crystal value suggests that the presence or absence of plastic deformation induced in the microstructure outside the contact impression does not significantly affect the supported contact stress.

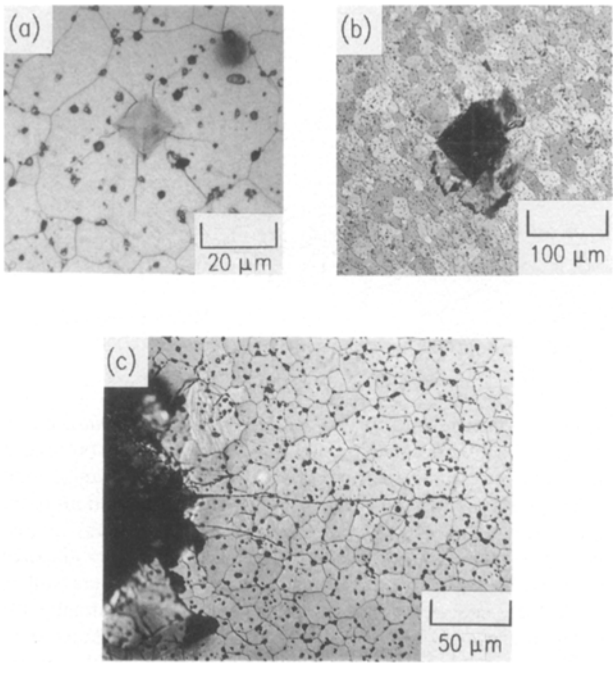

Figure 3 Optical micrographs (polarized reflected light) of indentation cracks in MgO. (a) 1 N indentation. (b) 50 N indentation. (c) Radial crack surface trace.

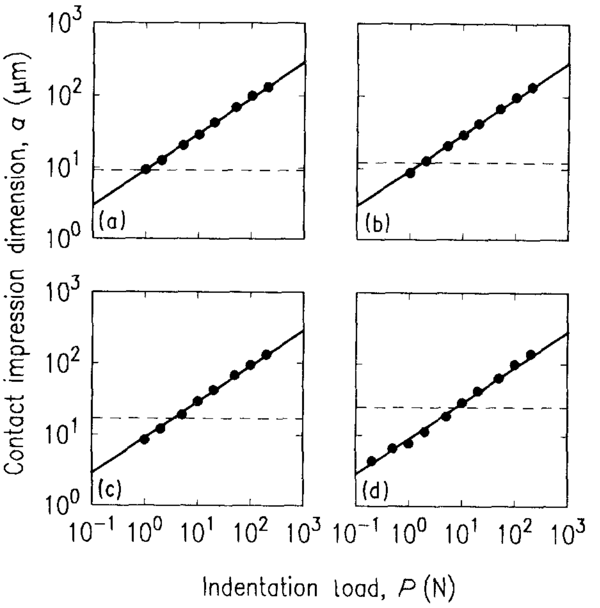

Figure 4 Indentation impression dimension a against indentation load P for polycrystalline MgO. The symbols represent the mean of 8–10 observations at each designated load, standard deviations are smaller than the symbol size. The solid lines are best fits, consistent with a constant hardness assumption (Equation 1). The dashed lines indicate the grain size λ. (a) $\lambda = 9.2$ μm; (b) $\lambda = 12$ μm; (c) $\lambda = 17$ μm; (d) $\lambda = 26$ μm.

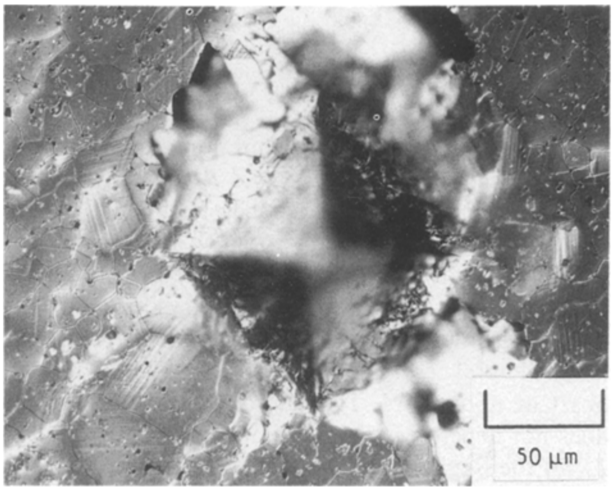

Figure 5 Optical micrograph (Nomarski contrast, reflected light) of slip traces adjacent to a 50 N indentation impression in polycrystalline MgO. Note the grain-localized nature of traces of a given orientation, and that some grains do not exhibit traces. The definite lateral crack development at this load is also evident.

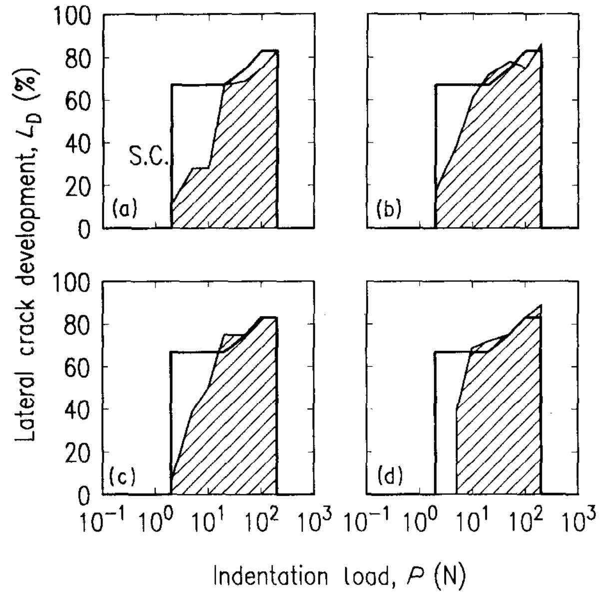

Figure 6 Lateral crack development L_D against indentation load P for MgO. Shaded regions indicate the response averaged over 4–5 indentations as a function of indentation load for each polycrystalline material. The solid line is the response observed for the single crystal. (a) $\lambda = 9.2$ µm; (b) $\lambda = 12$ µm; (c) $\lambda = 17$ µm; (d) $\lambda = 26$ µm.

Fig. 6 plots the lateral crack development L_D against indentation load P for the four polycrystalline materials. Lateral crack development is defined by [33]

$$L_D = (2V + R)/12 \qquad (2)$$

where V is the number of indentation quadrants containing visible lateral cracks, and R is the number of quadrants in which material has been removed by lateral cracks. The shaded regions in Fig. 6 represent L_D for the polycrystals, and the superimposed solid line represents L_D for the single crystal. Both the single-crystal and polycrystalline materials exhibit extensive lateral cracking which increases with P after an onset at about 2 N. The lateral crack development does not depend significantly on grain size, although L_D for the single crystal appears to be slightly less load dependent at low loads.

Micrographs of the fracture surfaces of the polycrystalline materials are shown in Fig. 7. The fracture surfaces were extremely uniform with no change in fracture morphology reflecting the location of the strength-controlling indentation flaw. The fracture is predominantly transgranular, with many changes in the local crack plane on length scales less than the grain size (although this is not reflected in the almost straight surface crack traces). Large (grain-scale) regions of planar transgranular (1 0 0) cleavage are separated by multifaceted, and sometimes re-entrant, regions of hackled non-planar fracture. (Far from the indentation the (1 0 0) cleavage will dominate.) The regions of disordered fracture indicate local grain orientations in which the (1 0 0) cleavage planes are not coplanar with the imposed macroscopic crack plane, and the crack adopts a "staircase" morphology to maintain local (1 0 0) cleavage. The severely jogged and kinked crack path leads to localized tractions acting across the macroscopic crack plane, shown schematically in Fig. 8a. These localized tractions or "ligamentary bridges" are similar in effect to those observed in polycrystalline Al_2O_3 [31, 32], except in

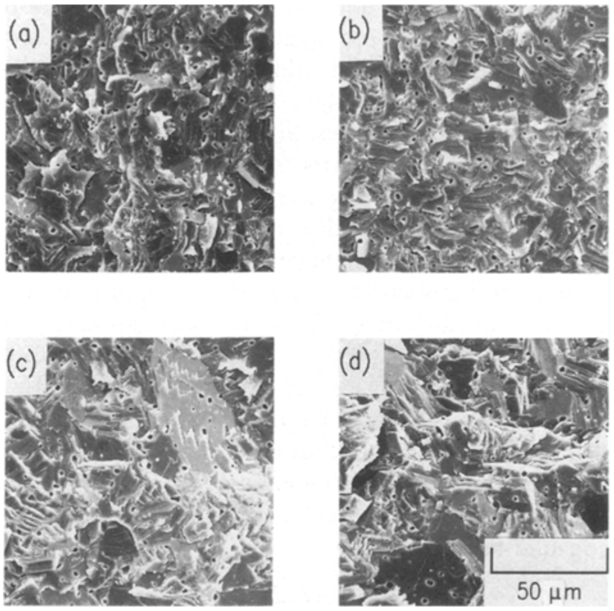

Figure 7 Scanning electron micrographs of the fracture surfaces of polycrystalline MgO. The convoluted nature of the fracture path, and the predominantly transgranular fracture are evident. Grain size increases from 9.2 to 26 µm in the sequence (a)–(d).

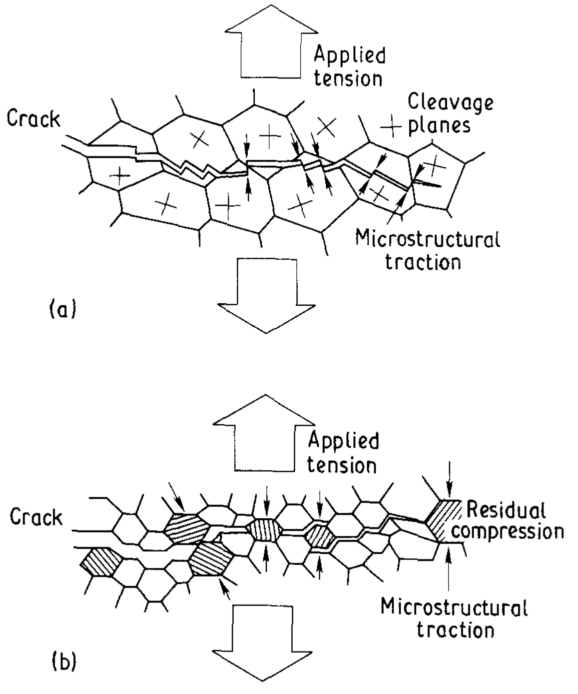

Figure 8 Schematic diagrams of microstructurally generated crack-bridging tractions leading to toughening in polycrystals. (a) Jogged, predominantly transgranular crack paths caused by anisotropic cleavage of single-crystal grains. The easy cleavage directions of the grains are indicated by crosses. The bridging tractions at jogs having significant components perpendicular to the imposed macroscopic crack path, and where the crack faces are still in contact, are indicated by arrows. (b) Discontinuous, predominantly intergranular crack path in a polycrystal with an inhomogeneous residual stress distribution. Compressive regions in the microstructure are indicated by shading. Bridging tractions are generated at frictionally interlocked grains under net compression and are indicated by arrows.

this case they derive from the anisotropic cleavage (and perhaps modulus [34]) of MgO and are localized within grains, whereas in Al_2O_3 the bridges are associated with residual stresses in the microstructure caused by anisotropic thermal expansion [5, 6], and are composed of whole grains or groups of grains [31, 32], Fig. 8b.

3. Theory

Based on the observations in Figs 3 to 7, the following sections develop expressions for the lengths of indentation radial cracks. The first section considers the effects of lateral cracking on radial crack lengths for materials with invariant fracture resistance. The expression thus derived is used to describe results from single-crystal MgO. The second section derives an expression for radial crack lengths in materials with increasing fracture resistance caused by crack-face tractions. This second expression is combined with the baseline description of the single-crystal behaviour to describe results from the polycrystalline materials.

3.1. Equilibrium crack lengths: Indentation field

Radial cracks are driven in an indentation stress field caused by the strain mismatch of a plastically deformed zone embedded in an elastically restraining matrix [35, 36]. An expression for the mechanical energy release rate $\mathcal{G}_a$ acting on the radial (Palmqvist, [29]) cracks in this stress field is [36]

$$\mathcal{G}_a = \beta P/l \tag{3}$$

where P is the indentation load, l is the surface trace of the radial crack (Fig. 2), and β is a numerical parameter characterizing the geometry of the indentation system. For geometrically similar systems β is a constant, dependent only on the modulus/hardness ratio of the material. Geometrical similarity of the elastic–plastic contact field under loading is indicated by the load-invariant hardness (Fig. 4) and the invariant ratio of dislocation rosette width to impression width [20]. Geometrical similarity of the final, unloaded indentation patterns is broken here as the degree of lateral cracking depends on P (Fig. 6). We assume here that changes in β are dominated by lateral crack effects, and that β decreases with increasing lateral crack development and hence with increasing indentation load. By analogy with expressions used earlier [33, 37] for the effect of lateral cracking on half-penny cracks, the expression for β we use here is

$$\beta = \beta_0/(1 + P/P_L) \tag{4}$$

in which β_0 is the geometry constant in the absence of any lateral cracking, and P_L is an indentation load scaling the effect of the load-dependent lateral cracking on the mismatch stress field driving the radial cracks. (It might also be argued that β should include a correction term in $a/(a + l)$ characterizing changes in radial crack geometry [36], leading to a P/l^4 dependence for $\mathcal{G}_a$ at $l \gg a$. In practice, however, the changes in the overall contact damage geometry mediated by the lateral cracks governs β.)

The original derivation related P_L to a volume constraint on the plastic deformation zone which decreased with increasing lateral crack development [37], leading to a decreased driving force for radial crack propagation with increasing indentation load. This is an indirect effect as the lateral crack development only influences the radial cracks via the deformation zone constraint. However, it is also possible that the lateral cracks have a direct effect by virtue of their shallow paths [22, 23, 29, 33], leading to an increased interference on radial crack propagation with increasing lateral crack development. In this case P_L is related to an area constraint on the radial crack path. Previous estimates suggest that P_L is about a factor of 100 greater than the indentation loads at which lateral cracks are first noticed [33].

The equilibrium condition for fracture in the frame of reference of the applied loading [32] (in this case the mismatch stress field) is

$$\mathcal{G}_a = R \tag{5}$$

When R takes a minimum, invariant value of 2γ the stable, equilibrium crack length l_0 is given by combining Equations 3–5

$$l_0 = l_0^L(P/P_L)/(1 + P/P_L) \tag{6}$$

which has asymptotic limits of

$$l_0 \rightarrow l_0^L = \beta_0 P_L/2\gamma \quad P \gg P_L \tag{7}$$

$$l_0 \rightarrow l_0^P = \beta_0 P/2\gamma \quad P \ll P_L \tag{8}$$

and where the subscript 0 indicates an absence of microstructural interaction. Fig. 9a plots Equation 6 and the asymptotes of Equations 7 and 8, showing the transition from a load-dependent radial crack length at low P, where lateral cracking is negligible, to a load-independent radial crack length at large P, where lateral cracks essentially absorb all the additional strain energy associated with the increasing indentation load.

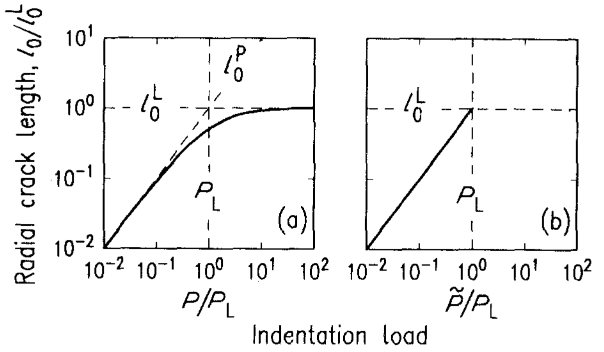

Figure 9 Plot of radial crack length against indentation load showing the effect of lateral cracking. (a) In the experimental co-ordinates of Equation 6 (solid line), demonstrating the approach to an invariant length at large loads. (The asymptotes of Equations 7 and 8 are shown as the dashed lines.) (b) In the compressed, effective co-ordinates of Equation 11 (solid line), demonstrating the collapse of the indentation scale, such that the crack length–indentation load relation is linear.

An alternative formulation of the load dependence of the radial crack length, which is more easily incorporated into the microstructural analysis to follow, leaves the geometry term invariant and creates an "effective" indentation load defined by combining Equations 3 and 4:

$$\tilde{P} = PP_L/(P + P_L) \qquad (9)$$

such that

$$\mathcal{G}_a = \beta_0 \tilde{P}/l \qquad (10)$$

This transformation collapses the P-scale onto a $\tilde{P}$-scale such that l_0 is linear in indentation load, in this case the effective load $\tilde{P}$

$$l_0 = \beta_0 \tilde{P}/2\gamma \qquad (11)$$

The non-linearity in the indentation field is now incorporated into $\tilde{P}$ which has asymptotic limits of

$$\tilde{P} \to P^+ \quad (P \ll P_L) \qquad (12a)$$

$$\tilde{P} \to P_L^- \quad (P \gg P_L) \qquad (12b)$$

Fig. 9b plots Equation 11 by using the transformation of Equation 9, demonstrating the collapse of the P-scale onto the $\tilde{P}$-scale to yield a linear dependence of the stable equilibrium crack length on the effective indentation load.

3.2. Equilibrium crack lengths: combined indentation and microstructural fields

The propagation of the radial cracks is impeded by two components of the fracture resistance. The first is the work associated with rupture of interatomic bonds, 2γ, and the second is the work associated with coming the crack-bridging tractions. The left side of Fig. 10 shows schematics of the tractions distributed over indentation half-penny and radial cracks. Close to the crack tips the crack walls are in close proximity and there are many regions of frictional interlocking and many traction points. Further behind the tips the number of traction points decreases as the crack opening increases, until a distance behind the tips is reached where the crack faces no longer interact and there are no traction points. In each case the crack shape is approximately semicircular, but because of the asymmetrical indentation wedge loading in the radial case the tractions extend only partly around the perimeter, compared with a full semicircular extension in the symmetric half-penny case.

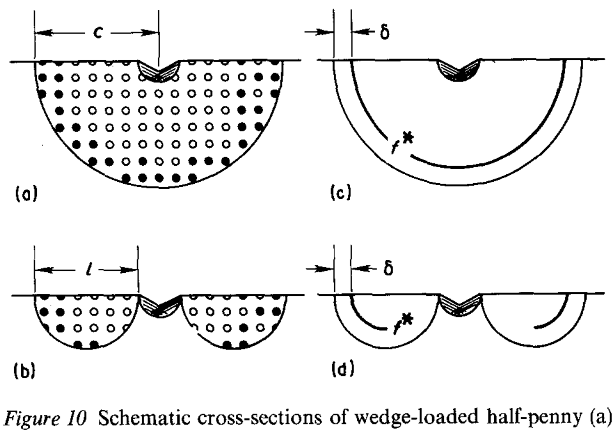

Figure 10 Schematic cross-sections of wedge-loaded half-penny (a) and radial (b) cracks bridged by localized crack-face tractions. Active traction sites adjacent to the crack tip are indicated by solid symbols; inactive sites remote from the tip, where the crack opening is large, are indicated by open symbols. The tractions are modelled as symmetric (c) and asymmetric (d) distributed lineforces in the calculation of the toughening effects.

The right side of Fig. 10 shows the traction distribution used in the calculation of the fracture resistance. The arrays of discrete point loadings are modelled as distributed line-force elements, imposed a fixed pinning distance behind the crack tip. The magnitudes of the line-force, f^*, and the pinning distance, δ, characterize the traction arrays integrated over co-ordinates parallel to the crack propagation direction, and averaged perpendicular to these co-ordinates [2, 3, 32]. Exact solutions [2, 38] for the stress intensity factors, K_μ, associated with the line-force elements in Fig. 10 are well approximated by forms more easily incorporated into indentation fracture analyses,

$$\begin{aligned} K_\mu &= -\mu f^* \delta^{-1/2}[1 - (\delta/c)^{3/2}] \quad &&\text{(half-penny, } c > \delta) \\ &= 0 &&(c \le \delta) \qquad (13) \end{aligned}$$

$$\begin{aligned} K_\mu &= -\mu f^* \delta^{-1/2}[1 - (\delta/l)^{1/2}] \quad &&\text{(radial, } l > \delta) \\ &= 0 &&(l \le \delta) \qquad (14) \end{aligned}$$

where μ is a numerical geometry constant of order 1. Equation 13 is that used previously in a strength analysis of polycrystalline Al_2O_3 [2], where the bridged cracks were assumed to be half-penny in shape. The difference in the crack-length dependence for the radial crack system, Equation 14, is a reflection of the loss of symmetry in this system. The restraining effect of the microstructural interactions increases rapidly after the first tractions are encountered ($l > \delta$) but eventually saturates to a steady-state restraint at large crack lengths ($l \gg \delta$).

Fracture resistance in the frame of reference of the applied loading is given by

$$R = [(2\gamma E)^{1/2} + T_\mu]^2/E \qquad (15)$$

where E is Young's modulus and T_μ is the toughening contribution from any microstructural influences [32]. Setting $T_\mu = -K_\mu$ [5, 6, 32], and combining Equations 14 and 15 yields the fracture resistance as a function of crack length

$$R/2\gamma = (R_\infty/2\gamma)\{1 - [1 - (R_\infty/2\gamma)^{-1/2}](\delta/l)^{1/2}\}^2 \qquad (16)$$

where the upper, asymptotic bound

$$R_\infty = [(2\gamma E)^{1/2} + \mu f^* \delta^{-1/2}]^2/E \qquad (17)$$

is the steady-state fracture resistance.

The stable equilibrium crack length, l_e, in the combined indentation and resistance fields is obtained by combining Equations 5, 10, 14, and 15

$$l_e = l^M[1 + (\tilde{P}/P^*)^{1/2}]^2 \qquad (18)$$

which has asymptotic limits of

$$l_e \to l^M = \beta_0 P^*/R_\infty \quad (\tilde{P} \ll P^*) \qquad (19)$$

$$l_e \to l^P = \beta_0 \tilde{P}/R_\infty \quad (\tilde{P} \gg P^*) \qquad (20)$$

where P^* is defined by

$$P^* = (\mu f^*)^2/\beta_0 E \qquad (21)$$

Fig. 11 plots Equation 18 and its asymptotic limits, showing the transition in the equilibrium crack length at P^* from the microstructurally dominated l^M-limit at low $\tilde{P}$ (Equation 19) where the fracture resistance is increasing rapidly, to the mismatch field dominated l^P-limit at large $\tilde{P}$ (Equation 20) where the fracture resistance has attained its upper steady-state value of R_∞. Also plotted in Fig. 11 is the l_0 response (Equation 11) applicable at low $\tilde{P}$ for cracks shorter than δ, where no toughening tractions are encountered and the fracture resistance has its lower steady-state value of 2γ. The complete crack length behaviour as a function of effective indentation load is given by the l_0 response for $l < \delta$ and transfers to the l_e response for $l > \delta$. (δ/l^M is approximately 2 in Fig. 11.)

The R-curve parameters $R_\infty/2\gamma$ and δ of Equation 16 are related to the load and crack length parameters characterizing the indentation response by

$$R_\infty/2\gamma = (P^*/l^M)/(P_L/l_0^L) \qquad (22)$$

from Equations 7 and 19, and

$$\delta = P^*[(P^*/l^M)^{1/2} - (P_L/l_0^L)^{1/2}]^{-2} \qquad (23)$$

from Equations 7, 17, 19, and 21, providing a means of estimating the fracture resistance variation from indentation crack length measurements. Although equations similar to Equations 13–21 have been used before, Equations 22 and 23 present the first deconvolution of the former to allow the $R(l)$ response to be determined explicitly.

4. Results

Fig. 12 plots the radial crack lengths measured for single-crystal MgO as a function of indentation load. Open symbols represent individual crack length measurements, solid symbols represent the mean crack length at a given indentation load, and the upper solid line represents the best fit to the data using Equation 6. The lower solid line represents the contact impression data over the same load range. The parameters characterizing the non-linear indentation crack length response are $P_L = 58.9$ N and $l_0^L = 624$ μm. Lateral crack effects are clearly significant in the range of indentation loads studied.

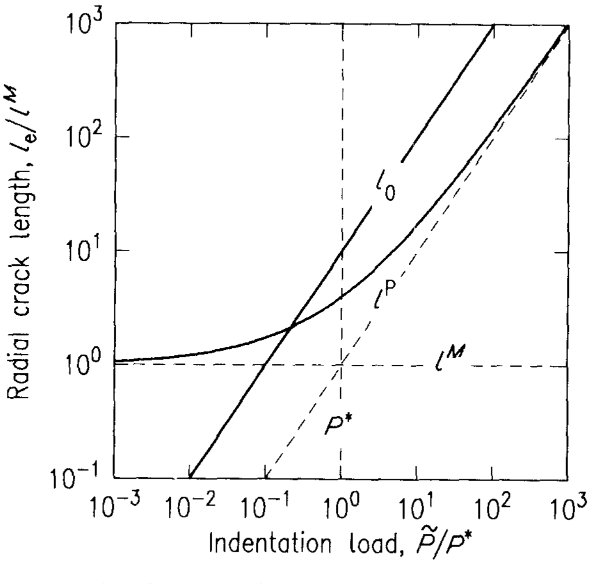

Figure 11 Plot of radial crack length against effective indentation load showing the effect of microstructural toughening. The full response (solid lines) approaches an invariant length at low loads (Equation 18), before the toughening mechanism is removed as the cracks encounter only single-crystal properties (Equation 11). (The asymptotes of Equations 19 and 20 are shown as the dashed lines.)

Fig. 13 plots the radial crack lengths measured for the polycrystalline MgO materials. Open symbols represent individual crack length measurements, solid symbols represent mean values, the solid lines represent best fits to the data using Equation 18, and the

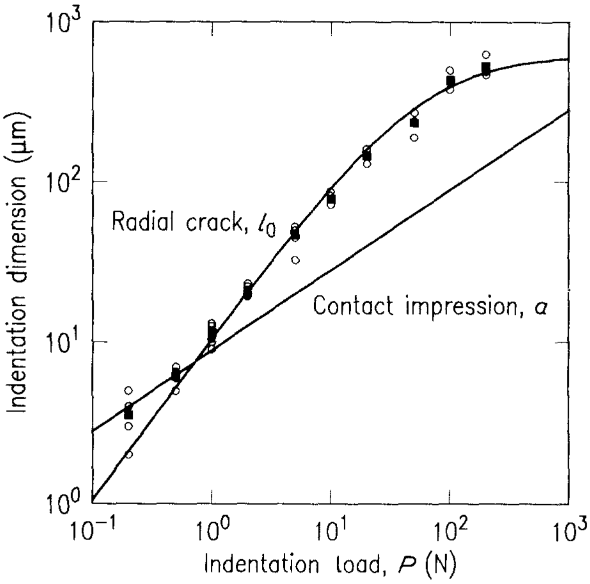

Figure 12 Radial crack length l_0 and contact impression a against indentation load P for single-crystal MgO (⟨1 0 0⟩ surface), demonstrating the effect of lateral cracking at large loads.

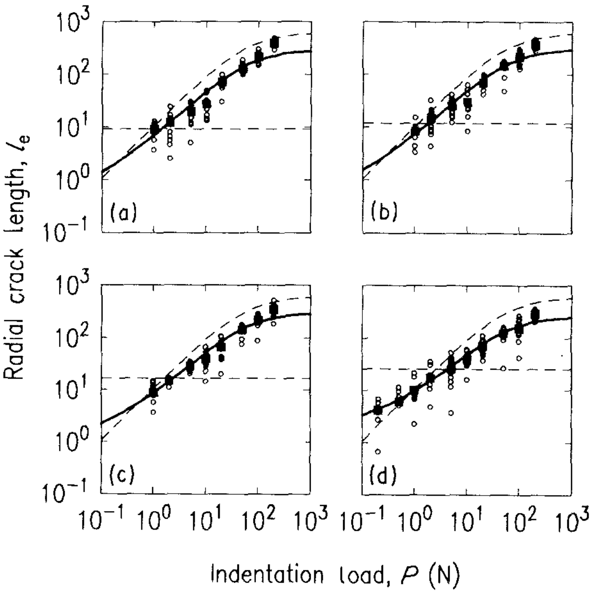

Figure 13 Radial crack length l_e against indentation load P for polycrystalline MgO, demonstrating the effect of microstructure. The dashed lines represent the single-crystal response (Fig. 12). The significantly shorter crack lengths for the polycrystalline materials are indicative of enhanced fracture resistance. (a) $\lambda = 9.2$ μm; (b) $\lambda = 12$ μm; (c) $\lambda = 17$ μm; (d) $\lambda = 26$ μm.

dashed lines the single-crystal response of Fig. 12. In no case was a best fit obtained by allowing some data to lie on the untoughened l_0 (single-crystal) branch of the full crack length response, even for very short cracks in the larger grain-sized materials. Over the range of indentation loads studied, the crack lengths for the polycrystalline materials are significantly shorter than those for the single-crystal material at the same indentation load, particularly for cracks longer than an average grain size (λ is indicated by the horizontal lines). Microstructural effects are clearly influencing crack propagation.

On the basis of the similar lateral crack development (Fig. 6) and hardness (Table I) exhibited by the single-crystal and polycrystalline materials, the P_L and l_0^L parameters used to convert P to $\tilde{P}$ (Equation 9) for use in Equation 18 for the polycrystalline materials were those determined from the base-line response of the single crystal. The P^* and l^M values thus derived are given in Table I. Using these values, Fig. 14 plots the appropriately normalized indentation crack length responses of all four materials, along with the universal curve of Equation 18, showing the significant non-linearity in the crack lengths at low indentation loads arising from microstructural effects. (The non-linear effects of lateral cracking at large loads have been normalized out by the use of the $\tilde{P}$, collapsing, transformation of Equation 9.)

Equations 22 and 23 were used to determine $R_\infty/2\gamma$ and δ from the crack length response parameters, and are given in Table I. Fig. 15 plots the R-curves thus obtained, using these parameters in Equation 16 and a value of $\gamma = 1.2\ \mathrm{J\,m^{-2}}$. (This is approximately that for (1 0 0) fracture of MgO determined by double cantilever beam measurements [17, 18], and is thus a lower-bound estimate.) Although the ultimate fracture resistance increment is approximately constant for all four materials ($R_\infty/2\gamma \simeq 2.5$), the length scale of the derived R-curves increases with increasing grain size. Fig. 16 shows this latter trend clearly, plotting δ against λ.

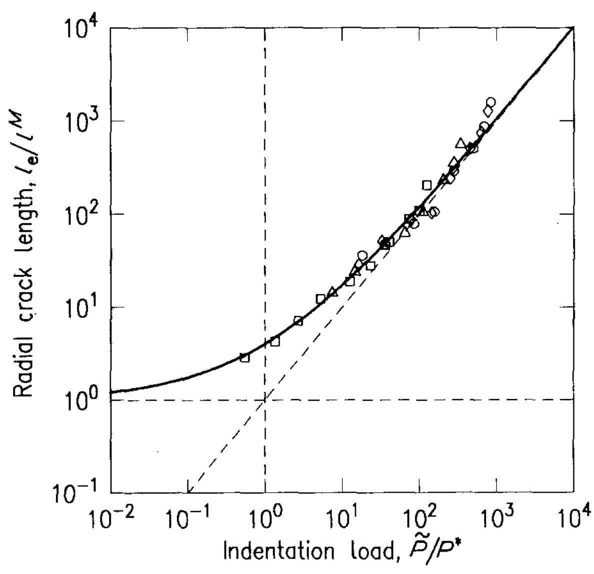

Figure 14 Normalized plot of radial crack length against indentation load for polycrystalline MgO, demonstrating the universal response consistent with Equation 18 (solid line). The symbols represent the mean crack lengths at each indentation load taken from Fig. 13, different symbols represent different grain sizes.

5. Discussion

The dominant effect of increasing grain size on the indentation fracture response of the MgO materials examined here is to increase the length scale δ over which the fracture resistance rises to a steady-state value (Table I, Figs 15 and 16). The maximum increase in fracture resistance increases weakly with grain size (Table I, Fig. 15), although extrapolation of the data to small grain sizes implies that a minimum grain size is required to generate the microstructural toughening (Fig. 16). These three findings are consistent with the interaction sketched in Fig. 8a, given that there is a grain-size-independent maximum deviation of the local crack path from the imposed global crack plane.

An invariant maximum deviation yields a constant density of jogs for a given crack-plane : cleavage-plane

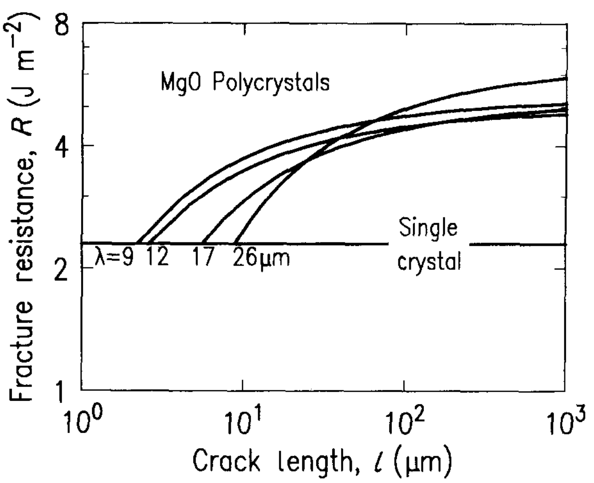

Figure 15 Fracture resistance R against crack length l for MgO using the formulation of Equation 16 and the scaling parameters determined from the indentation tests (Table I). The single-crystal response is invariant and serves to calibrate the absolute values of the polycrystalline responses.

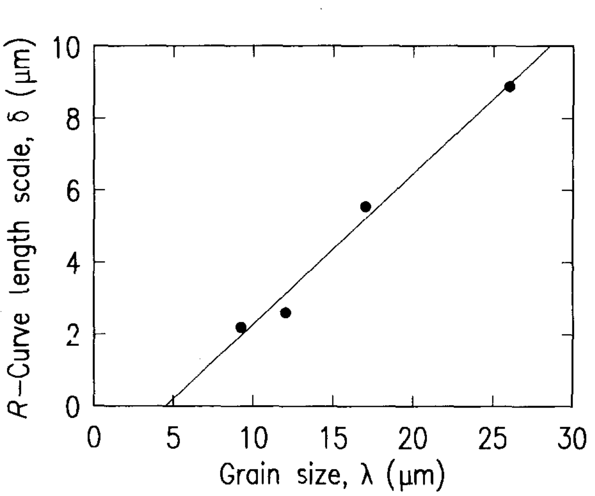

Figure 16 Plot of the R-curve length-scale parameter δ against grain size λ for polycrystalline MgO. The solid line is a best fit to the data and indicates a removal of the toughening mechanism for grain sizes less than ~ 5 μm.

orientation, and hence the jog density changes as the crack traverses different grains. The density of jogs within a grain increases to a maximum as the imposed crack plane approaches a 45° orientation to the two appropriate {1 0 0} cleavage planes. However, the density of crack-face traction sites approaches a minimum at this orientation: the density of traction sites is maximized as the crack plane approaches (but does not equal) a 0° orientation, as in this case high-angle, frictionally interlocked jogs are formed on one of the cleavage planes. Additionally, grain-boundary jogs are generated as the crack encounters a new cleavage orientation, and these jogs will generally reduce the angle of the local crack path with the imposed global crack plane.

For small grain sizes the crack never forms high-angle jogs, as a grain-boundary jog will always form before the maximum deviation is reached. No tractions, and hence no toughening are thus expected below a minimum grain size. Above this minimum, the maximum deviation is reached within a grain before a grain-boundary jog can form, and high-angle, frictionally interlocked jogs form, resulting in toughening. Increasing the grain size (relative to the invariant maximum deviation) results in a greater density of high-angle jogs and density of traction sites, and thus a greater absolute distance behind the crack tip at which bridging is maintained. The length scale parameter δ is a measure of this distance and thus increases with grain size. If the frictional stress exerted by a traction site falls off rapidly with increasing crack opening [3, 5, 6, 31–33], the integrated effect of a fully formed bridging zone is only weakly sensitive to grain size. The steady-state fracture resistance R_∞ is a measure of this integrated effect and thus increases slowly with grain size.

It should be noted that "steps" on the fracture surfaces of materials with strong tendencies to cleavage have been suggested before as a toughening mechanism: increases in the fracture resistance of LiF cantilever beam specimens were correlated with the number of steps on the fracture surface [17]; the increased fracture resistance of MgO cantilever beam specimens tested in water relative to those tested in formamide was explained by noting that steps were observed only on the former [39]; and, the larger fracture resistance of polycrystalline MgO bend bars, compared with the single-crystal value, was suggested to arise from grain-boundary interactions increasing the number and size of steps on the fracture surface [40]. A feature of all these works, however, was that the increased energy required to propagate the crack in the average plane was associated with the formation of the steps, by deviation of the crack out of the plane, rather than by interaction of steps across the plane. In this sense the ideas are reminiscent of toughening by "crack deflection" [41], rather than by "crack bridging" [31].

Previous estimates of the steady-state fracture resistance of comparable MgO polycrystals include 4–16 $\mathrm{J\,m^{-2}}$, depending on grain size (7–23 μm) [40]; 4–12 $\mathrm{J\,m^{-2}}$, depending on crack length (20 μm grain size) [42]; 5 $\mathrm{J\,m^{-2}}$, independent of crack length (25 μm grain size) [43]; and 5 and 11 $\mathrm{J\,m^{-2}}$ depending on grain size (2 and 10 μm) [16] (all determined by notched beam tests). These compare with the lower bound estimates here of 5–6.4 $\mathrm{J\,m^{-2}}$. Magnitudes of bridging tractions have been estimated to be in the range 100–400 MPa, using somewhat more sophisticated models of the toughening process [3, 32]. The parameter f^*/δ provides a measure of the tractions here, and, using Equations 7 and 21, values in the range 280–450 MPa are obtained for these MgO materials. The indentation fracture model developed thus appears capable of generating absolute estimates of fracture resistance (once calibrated by the single-crystal data). Of course, goodness of fit between the analysis and the data is not proof of the model.

Hardness measurements obtained by other workers are greater than those observed here: 8 GPa for a chemically polished surface and 11 GPa for a ground surface [13]; 9.5 GPa on a (1 0 0) single-crystal surface [23]; and, 8.5 GPa on a single-crystal surface [24]. Possible reasons for the discrepancies may lie in differences in porosity, but more likely in differences in surface preparation.

Two other polycrystalline ceramics in which the toughening mechanism of Fig. 8a is possibly operating are Y_2O_3 and $MgAl_2O_4$. Examination of the fracture surface of mixed-phase cubic + hexagonal Y_2O_3 shows much greater convolution than that on the single-phase cubic material [30]. Indentation crack length measurements (again taking the lateral crack influence into account) [33], suggest a greater steady-state fracture resistance for the mixed-phase material. No change in fracture resistance with crack length was discerned for these materials, probably as a result of the small grain sizes. Straight radial crack surface traces were also observed in Y_2O_3, reinforcing that this observation is not a good indicator of a general lack of microstructural interaction. Polycrystalline $MgAl_2O_4$ shows dramatic increases in steady-state fracture resistance (determined by double cantilever beam tests) for materials displaying mixer inter- and transgranular failure, above those displaying predominantly intergranular failure and less convoluted fracture surfaces [44]. An inference is that transgranular failure elements contain frictionally interlocked jogs as a consequence of the lower (1 0 0) cleavage resistance of single-crystal $MgAl_2O_4$.

Regardless of the toughening mechanism, the analysis developed here for stable crack lengths in the presence of an R-curve should be generally applicable. In large-grained polycrystalline Al_2O_3, indentation radial cracks [1, 32] and spontaneous (micro)cracks generated adjacent to expanding grains [5, 6] should approach invariant values as the indentation load is decreased or the magnitude of the thermally induced expansion strain is reduced. Cracks generated at martensitically transforming ZrO_2 particles in Al_2O_3–ZrO_2 or Al_2TiO_5–ZrO_2 composites should also show an approach to invariant lengths as the temperature change or stress required to induce the transformation are reduced [45]. Sintering bodies containing dense inclusions generate stabilizing fracture fields about the inclusion, and cracks generated in these cases [46, 47] should also approach invariant lengths as the difference in the densification rate of the inclusion and the matrix, or the inclusion size, is reduced. In MgO itself, cracks nucleated and initiated by pileup of dislocations in macroscopically stressed components will be stabilized by the jog interaction; an example is observed in [28].

The importance of these cases is that they are all examples of "intrinsic" or "natural" flaws. If there is a minimum allowed crack length in a material, an implication is that there will be a maximum sustainable stress. Hence, an understanding of the interaction between a stabilizing field and an increasing fracture resistance is crucial to the development of stronger materials.

6. Summary

1. Indentations in polycrystalline MgO were characterized by a zone of plasticity around the remnant contact impression, well-developed shallow lateral cracks, and radial (Palmqvist) cracks with predominantly transgranular surface traces.

2. The hardness and lateral crack development of the polycrystals were marginally depressed from those observed for the single-crystal MgO and independent of grain size, indicating a minor role for the extent of plastic deformation in determining the contact stress field.

3. Radial crack lengths in polycrystalline MgO were significantly decreased compared with those in the single crystal. Fracture surface observations suggested that the enhancement of the fracture resistance in polycrystals was due to frictional interlocking of jogs across the crack plane.

4. Expressions were developed for the mechanical energy release rate of the radial cracks, taking lateral crack interactions into account, and for the fracture resistance, modelling the discrete closing tractions of the jogs as distributed line force elements. The combination of these expressions allowed the radial crack lengths as a function of indentation load to be described.

5. The explicit deconvolution of the fitting parameters used in the radial crack description permitted the fracture resistance variation with crack length for the polycrystalline materials to be estimated. The steady-state fracture resistance was found to be relatively independent of grain size, and, above a "threshold" of approximately 5 μm, the length scale of the fracture resistance rise with crack length was found to increase with grain size.

Acknowledgements

The authors thank M. D. Thouless for helpful conversations on aspects of the modelling and P. R. Duncombe for assistance with the heat treatment and X-ray diffraction of specimens.

References

1. R. F. COOK, B. R. LAWN and C. J. FAIRBANKS, *J. Amer. Ceram. Soc.* **68** (1985) 604.
2. R. F. COOK, in "Advanced structural ceramics", edited by P. F. Becher, M. V. Swain and S. Somiya (Materials Research Society, Pittsburgh, 1987) p. 199.
3. R. F. COOK, C. J. FAIRBANKS, B. R. LAWN and Y.-W. MAI, *J. Mater. Res.* **2** (1987) 345.
4. R. F. COOK and D. R. CLARKE, *Acta Metall.* **36** (1988) 555.
5. S. J. BENNISON and B. R. LAWN, *J. Mater. Sci.* **24** (1989) 3169.
6. Idem., *Acta Metall.* **37** (1989) 2659.
7. P. CHANTIKUL, S. J. BENNISON and B. R. LAWN, *J. Amer. Ceram. Soc.* **73** (1990) 2419.
8. M. V. SWAIN and R. H. J. HANNINK, in "Science and Technology of Zirconia II", edited by N. Claussen, M. Rühle and A. H. Heuer (American Ceramic Society, Columbus, 1984) p. 225.
9. D. B. MARSHALL, *J. Amer. Ceram. Soc.* **69** (1986) 173.
10. N. CLAUSSEN, K.-L. WIESSKOPF and M. RÜHLE, *Ibid.* **69** (1986) 288.
11. M. V. SWAIN and L. R. F. ROSE, *Ibid.* **69** (1986) 511.
12. T. SHIMADA, K. NAGATA, M. HASHIBA, E. MIURA, T. ONO and Y. NURISHI, in "Science and Technology of zirconia III", edited by S. Somiya, N. Yamamoto and H. Hanagida (American Ceramic Society, Westerville, 1988) p. 397.
13. R. W. RICE, *J. Amer. Ceram. Soc.* **56** (1973) 536.
14. A. U. DANIELS, Jr, R. C. LOWIE, Jr, R. L. LIBBY and I. B. CUTLER, *Ibid.* **45** (1962) 282.
15. R. M. SPRIGGS, L. A. BRISSETTE and T. VASILOS, *Ibid.* **47** (1964) 417.
16. J. B. KESSLER, J. E. RITTER, Jr and R. W. RICE, in "Surfaces and Interfaces of Glass and Ceramics", edited by V. D. Fréchette, W. C. LaCourse and V. L. Burdick (Plenum, New York, 1974) p. 529.
17. J. J. GILMAN, *J. Appl. Phys.* **31** (1960) 2208.
18. A. R. C. WESTWOOD and D. L. GOLDHEIM, *Ibid.* **34** (1963) 3335.
19. A. S. KEH, J. C. M. LI and Y. T. CHOU, *Acta Metall.* **7** (1959) 694.
20. A. S. KEH, *J. Appl. Phys.* **31** (1960) 1538.
21. R. W. DAVIDGE, *J. Mater. Sci.* **2** (1967) 339.
22. D. G. RICKERBY, B. N. PRAMILA BAI and N. H. MACMILLAN, *Ibid.* **14** (1979) 1807.
23. D. G. RICKERBY and N. H. MACMILLAN, *Ibid.* **14** (1979) 2435.
24. P. J. BURNETT and T. F. PAGE, *J. Mater. Sci. Lett.* **4** (1985) 1364.
25. C. A. BROOKES and J. D. J. ROSSI, *Eur. Appl. Res. Rep. Nucl. Sci. Technol. Section* **7** (1987) 1147.
26. YU. S. BOYARSKAYA, D. Z. GRABKO and M. S. KATS, *J. Mater. Sci.* **25** (1990) 3611.
27. R. J. STOKES, T. L. JOHNSTON and C. H. LI, *Phil. Mag.* **4** (1959) 920.
28. T. L. JOHNSTON, R. J. STOKES and C. H. LI, *Ibid.* **7** (1962) 23.
29. R. F. COOK and G. M. PHARR, *J. Amer. Ceram. Soc.* **73** (1990) 787.
30. R. F. COOK, M. R. PASCUCCI and E. G. LINIGER, unpublished work.
31. P. L. SWANSON, C. J. FAIRBANKS, B. R. LAWN, Y.-W. MAI and B. J. HOCKEY, *J. Amer. Ceram. Soc.* **70** (1987) 279.
32. R. F. COOK, *Acta Metall.* **38** (1990) 1083.
33. R. F. COOK, M. R. PASCUCCI and W. H. RHODES, *J. Amer. Ceram. Soc.* **73** (1990) 1873.
34. R. P. INGEL and D. LEWIS, *Ibid.* **71** (1988) 265.
35. B. R. LAWN, A. G. EVANS and D. B. MARSHALL, *Ibid.* **63** (1980) 574.
36. M. T. LAUGIER, *Ibid.* **68** (1985) C-51.
37. R. F. COOK and D. H. ROACH, *J. Mater. Res.* **1** (1986) 589.
38. H. TADA, P. PARIS and G. R. IRWIN, "The stress analysis of cracks handbook", (Del Research, St Louis, 1973) pp. 24-3, 24-4.
39. D. A. SHOCKEY and G. W. GROVES, *J. Amer. Ceram. Soc.* **52** (1969) 82.
40. F. J. P. CLARKE, H. G. TATTERSALL and G. TAPPIN, *Proc. Brit. Ceram. Soc.* no. 6. "Mechanical properties of non-

metallic crystals and polycrystals" (British Ceramic Society, Stoke-on-Trent, 1966) p. 163.

41. K. T. FABER and A. G. EVANS, *Acta Metall.* **31** (1983) 565.
42. A. G. EVANS and R. W. DAVIDGE, *Phil. Mag.* **20** (1969) 373.
43. A. G. EVANS, D. GILLING, and R. W. DAVIDGE, *J. Mater. Sci.* **5** (1970) 187.
44. R. L. STEWART, M. IWASA and R. C. BRADT, *J. Amer. Ceram. Soc.* **64** (1981) C-22.
45. D. J. GREEN, R. H. J. HANNINK and M. V. SWAIN, "Transformation toughening of ceramics" (CRC Press, Boca Raton, 1989) Ch. 5.
46. C. P. OSTERTAG, *J. Amer. Ceram. Soc.* **70** (1987) C-355.
47. L. C. STEARNS, M. P. HARMER and H. M. CHAN, *Ibid.* **73** (1990) 2740.

Received 8 May
and accepted 12 September 1991